

Key Points:

- The Lagrangian transport time scales in the Dutch Wadden Sea are typically 1.7 times smaller in autumn-winter than in to spring-summer
- The seasonal and interannual variability of the Lagrangian transport time scales is attributed to the local wind
- The winter interannual variations are well explained by North Atlantic large-scale atmospheric patterns

Supporting Information:

Supporting Information may be found in the online version of this article.

Correspondence to:

M. Duran-Matute,
m.duran.matute@tue.nl

Citation:

Fajardo-Urbina, J. M., Arts, G., Gräwe, U., Clercx, H. J. H., Gerkema, T., & Duran-Matute, M. (2023). Atmospherically driven seasonal and interannual variability in the Lagrangian transport time scales of a multiple-inlet coastal system. *Journal of Geophysical Research: Oceans*, 128, e2022JC019522. <https://doi.org/10.1029/2022JC019522>

Received 28 NOV 2022

Accepted 18 JUN 2023

Author Contributions:

Conceptualization: Jeancarlo M.

Fajardo-Urbina, Gijs Arts, Herman J. H. Clercx, Theo Gerkema, Matias Duran-Matute

Data curation: Jeancarlo M.

Fajardo-Urbina

Formal analysis: Jeancarlo M. Fajardo-Urbina, Gijs Arts

Funding acquisition: Theo Gerkema, Matias Duran-Matute

Investigation: Jeancarlo M. Fajardo-Urbina, Gijs Arts

Methodology: Jeancarlo M. Fajardo-Urbina, Gijs Arts, Ulf Gräwe, Matias Duran-Matute

© 2023. The Authors.

This is an open access article under the terms of the [Creative Commons Attribution License](https://creativecommons.org/licenses/by/4.0/), which permits use, distribution and reproduction in any medium, provided the original work is properly cited.

Atmospherically Driven Seasonal and Interannual Variability in the Lagrangian Transport Time Scales of a Multiple-Inlet Coastal System

Jeancarlo M. Fajardo-Urbina¹ , Gijs Arts¹ , Ulf Gräwe², Herman J. H. Clercx¹, Theo Gerkema³ , and Matias Duran-Matute¹ 

¹Fluids and Flows Group, J.M. Burgers Center for Fluid Dynamics, Department of Applied Physics and Science Education, Eindhoven University of Technology, Eindhoven, The Netherlands, ²Leibniz Institute for Baltic Sea Research Warnemünde, Rostock, Germany, ³Department of Estuarine and Delta Systems, NIOZ Royal Netherlands Institute for Sea Research, Yerseke, The Netherlands

Abstract Intense short-term wind events can flush multiple-inlet systems and even renew the water entirely. Nonetheless, little is known about the effect of wind variations at seasonal and interannual scales on the flushing of such systems. Here, we computed two Lagrangian transport time scales (LTTS), the residence and exposure times, for a multiple-inlet system (the Dutch Wadden Sea) over 36 years using a realistic numerical model simulation. Our results reveal pronounced seasonal and interannual variability in both system-wide LTTS. The seasonality of the LTTS is strongly anti-correlated to the wind energy from the prevailing directions, which are from the southwesterly quadrant and coincidentally aligned with the geographical orientation of the system. This wind energy, which is stronger in autumn-winter than in spring-summer, triggers strong flushing (and hence low values of the LTTS) during autumn-winter. The North Atlantic Oscillation (NAO) and the Scandinavia Pattern (SCAN) are shown to be the main drivers of interannual variability in the local wind and, ultimately, in both LTTS. However, this coupling is much more efficient during autumn-winter when these patterns show larger values and variations. During these seasons, a positive NAO and a negative SCAN induce stronger winds in the prevailing directions, enhancing the flushing efficiency of the system. The opposite happens during positive SCAN and negative NAO, when weaker flushing during autumn-winter is observed. Thus, large-scale atmospheric patterns strongly affect the interannual variability in flushing and are potential drivers of the long-term ecology and functioning of multiple-inlet systems.

Plain Language Summary In multiple-inlet coastal systems, strong wind events efficiently renew the water in these systems. In this paper, we investigate if the flushing of such systems has also a marked response to wind variability at longer time scales. To quantify the flushing, we compute the time that particles spend in the system before leaving it (known as the residence time), and the total time they spend within it considering future returns (known as the exposure time). Our 36-year simulation of the hydrodynamics of the Dutch Wadden Sea (DWS) shows that the wind induces seasonal and interannual variations in both spatially-averaged quantities. The seasonality is related to the wind energy from the dominant directions, which is much larger during autumn-winter than during spring-summer. This variation leads to a reduction of both time scales by, on average, a factor of 1.7 from spring-summer to autumn-winter. Two well-known North Atlantic large-scale atmospheric patterns, primarily active during autumn-winter, induce interannual variations in the wind and consequently in both time scales. Thus, future changes in these patterns could strongly affect water transport and the ecology of the DWS. Similar situations are likely to occur in other multiple-inlet systems.

1. Introduction

Transport time scales (TTS), such as the residence, exposure, transit, age, and flushing times (Monsen et al., 2002; Zimmerman, 1976), are measures for the efficiency of transport and exchange of water or freshwater content within a water body system and with its surroundings (Cucco et al., 2009; Duran-Matute et al., 2014; Rayson et al., 2016; Xiong et al., 2021). They also serve to estimate the time that a substance, like dissolved nitrogen, takes to be transported off-shore from high-productivity coastal regions (Hailegeorgis et al., 2021); to understand the variability of the mineralization rates of organic matter in sediments (den Heyer & Kalff, 1998); to explain

Project Administration: Matias Duran-Matute
Resources: Ulf Gräwe, Theo Gerkema
Software: Ulf Gräwe
Supervision: Herman J. H. Clercx, Theo Gerkema, Matias Duran-Matute
Validation: Jeancarlo M. Fajardo-Urbina
Writing – original draft: Jeancarlo M. Fajardo-Urbina
Writing – review & editing: Ulf Gräwe, Herman J. H. Clercx, Theo Gerkema, Matias Duran-Matute

regional differences of nutrient and eutrophication levels (González et al., 2008; Schwichtenberg et al., 2017); and as a first-order estimation of the exposure of a region (e.g., a protected area) to pollutants (Patgaonkar et al., 2012; Pawlowicz et al., 2019; Soomere et al., 2011).

Depending on a coastal system's particularities, the TTS's variability can be highly affected by tides, freshwater discharge, gravitational circulation, winds, and other factors. The influence of some of these forcing mechanisms on the intra-annual and the seasonal variability of the TTS has been explored in bights (Zhang et al., 2010), bays (Dippner et al., 2019; Jiang et al., 2019) and lakes (Cimattoribus et al., 2019). However, these studies were based on just 1–2 years of data, and thus, a robust relationship of the seasonality with the local forcing cannot be expected if there is a marked interannual variability.

A realistic simulation covering 32 years was used by Du and Shen (2016) to study the residence time in the Chesapeake Bay. The seasonal, monthly, and interannual variability of the system-wide Eulerian residence time were found to be mainly controlled by the freshwater discharge. They also found that downstream and upstream winds reduce the residence time in the eastern side of the Bay, whereas only upstream winds increase the residence time in the western part. This means that in this single-inlet system winds from different directions can trigger complex patterns in the TTS, but they do not necessarily induce a net wind-driven overall transport in the system when, for example, variations of opposite signs in the TTS are observed on both sides of this Bay.

Single-inlet systems contrast with multiple-inlet systems because, in the latter, winds from specific directions are very efficient in forcing net residual transport across the system (Duran-Matute et al., 2016; Herrling & Winter 2015; Li, 2013). Due to this effect, the influence of other forcing mechanisms can become of secondary importance during strong wind conditions. Thus, winds in multiple-inlet systems can strongly modify the TTS at local, inter-basin, and system-wide scales. This effect has been observed in different multiple-inlet systems using numerical simulations. Cucco and Umgiesser (2006) showed that, in the Venice lagoon, strong northeasterly bora winds (of around 12 m/s) lead to a fully wind-driven dominated system, to a reduction of the system-averaged residence time by a factor of 3, and to a negligible return flow. In the Dutch Wadden Sea (DWS), strong winds exceeding 10 m/s, and aligned with the geographical orientation of the system, induce a wind-driven flow that reduces the system-wide flushing time of freshwater discharge by a factor of 10–15 (Donatelli et al., 2022a; Duran-Matute et al., 2014). Similar strong winds as in the previous cases, also reduced the monthly-average residence time by about a factor of 2 in the Virginia Coast Reserve (Safak et al., 2015); and the daily-average Lagrangian residence time (for particles released every 1h during a particular day) in areas located between the inlets of the Barnegat Bay-Little Egg Harbor estuary by a factor between 2 and 4 (Defne & Ganju, 2015).

Until now, the previous studies linking TTS to wind in multiple-inlet systems focused on idealized fixed wind conditions (e.g., Cucco & Umgiesser, 2006), synoptic-scale events (e.g., Duran-Matute et al., 2014; Safak et al., 2015) and annual statistics (e.g., Donatelli et al., 2022a). In the latter case, Donatelli et al. (2022a) showed that sporadic strong high-frequency winds (with time scales in the order of days) could impact the annual TTS averages in the DWS, but also the long-term values (mean or median representative of their 11-year simulation). However, they did not isolate the effect of high- and low-frequency winds (with time scales of months or longer) on the TTS to unequivocally attribute the changes in the annual and long-term TTS to high-frequency wind events. The relevance of the low-frequency variability is further suggested by the fact that monthly and multi-decadal sea level variability in the North Sea region is modulated by large-scale atmospheric patterns, which are represented by the North Atlantic Oscillation (NAO), the East Atlantic Pattern (EAP) and the Scandinavia Pattern (SCAN) (Chafik et al., 2017; Frederikse & Gerkema, 2018). Therefore, we investigate if and how much these large-scale atmospheric patterns affect the TTS in the DWS.

Our goal is to determine the low-frequency variability (i.e., the seasonality and interannual variations) of the Lagrangian TTS (LTTS), particularly the residence and exposure times, in a multiple-inlet system. Moreover, we aim to correlate their system-wide behavior with the wind and large-scale atmospheric patterns. The region of analysis covers most of the DWS (Figure 1): a UNESCO world heritage site and a complex multiple-inlet system. Due to the lack and the difficulty of acquiring observed Lagrangian data in shallow coastal regions, the results are based on a realistic 36-year simulation (1980–2015) of the DWS, combined with particle tracking. The simulation consists of an offline coupling of the General Estuarine Transport Model (GETM; Burchard & Bolding, 2002) with the Probably A Really Efficient Lagrangian Simulator (Parcels) v2.1.1 (Delandmeter & Van Sebille, 2019; Lange & van Sebille, 2017).

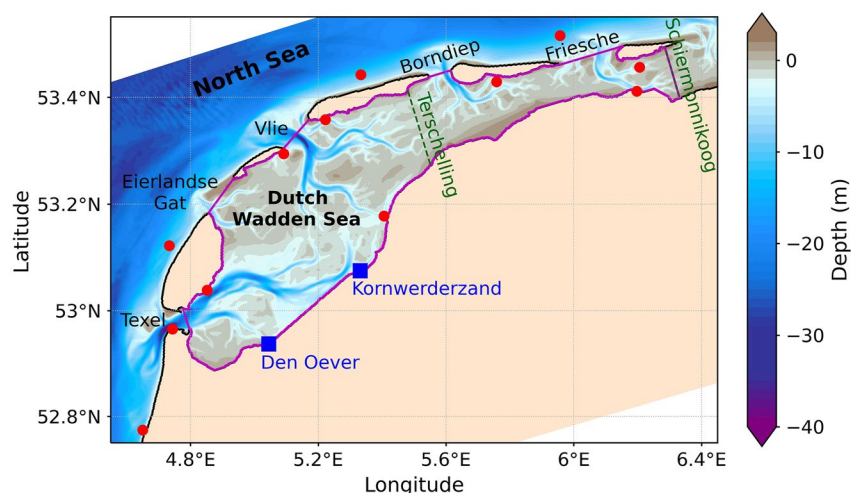


Figure 1. Map of the region of interest. The magenta contour surrounds most of the DWS and denotes the region where particles were deployed. The names of the five inlets are indicated in black. The Schiermonnikoog and the Terschelling watersheds are marked in green. The location of the two main sluices (squares) and their names are depicted in blue. The stations employed for the validation with the sea surface height (SSH) are shown with red dots. Two stations for SSH are located in the sluices, so they are also represented by blue squares.

2. Data and Methods

2.1. Numerical Models

2.1.1. Eulerian Model

Currents, sea level, salinity, temperature, and density are obtained through 3D baroclinic numerical simulations performed using GETM. The setup is based on four nested models, with the DWS numerical domain as the end-member (see Text S1 and Figure S1 in Supporting Information S1 for details of the model hierarchy). The DWS domain is discretized using an equidistant grid of 200 m resolution using the Rijksdriehoek projection (the standard projection employed by the Dutch Government) in the horizontal and 25 layers in the vertical. The bathymetry was built based on the measurements closest in time to 2009–2010 (see Duran-Matute et al., 2014, for details), and the resulting map was kept fixed throughout the 36-year simulation. This was done intentionally to remove the effects of bathymetry variations on the hydrodynamics of the system and to focus on the role of the atmospheric forcing. The meteorological forcing was taken from the data set “Uncertainties in Ensembles of Regional Reanalyses” (UERRA; Ridal et al., 2017), which has a spatial resolution of 11 km and a temporal resolution of 1 hr. The freshwater discharge through the Den Oever and Kornwerderzand sluices and 10 other smaller ones was reconstructed based on data collected by Rijkswaterstaat (part of the Dutch Ministry of Infrastructure and Water Management). The resulting data have a temporal resolution of 12 min (see Duran-Matute et al., 2014, for details). In the model, the flooding and drying are done in such a way that a very thin layer of fluid artificially always remains (0.15 m for our setup). When the total water depth approaches this value, simplified physics in the momentum equations are considered (Burchard & Bolding, 2002). Our model configuration is almost identical to those employed by Donatelli et al. (2022a); Donatelli et al. (2022b), but the simulation here spans 36 years instead of 11 years.

The skill of the model to simulate the hydrodynamics in the DWS was evaluated for previous implementations of our numerical setup. The simulation performed by Duran-Matute et al. (2014) for the years 2009–2010 reproduced quite well the observed sea surface height (SSH) at 14 tidal stations, the time series of sea surface salinity and temperature at a station located in the northern part of the Texel inlet, and the total volume transport across this inlet. Sassi et al. (2016) carried out a deeper comparison with velocity profile data collected beneath a ferry that crosses the Texel inlet during the year 2009. This comparison showed good performance for the simulated total transport, depth-averaged currents, and currents along the Texel inlet. For a larger domain that covered the whole Wadden Sea (which includes our numerical domain), Gräwe et al. (2016) found that numerical simulations for the years 2009–2011 reproduced quite well the observed sea surface height, sea surface temperature, sea

surface salinity, sea surface currents, currents along different transects, and total volume transport through two tidal inlets. Based on all this evidence, we consider that the ability of the model in reproducing the hydrodynamics should be reflected in our Lagrangian simulation (see Section 2.1.2) employed to study the variability of the LTTS in the DWS in a realistic way. In Text S2 in Supporting Information S1, we contrast our numerical results with the SSH measured at 14 tidal stations (Figure 1) to show that our setup performs as well as the previous ones.

2.1.2. Lagrangian Model

Passive particle trajectories were obtained offline by feeding vertically-averaged velocities every 20 min from the GETM simulation to Parcels to capture the effects of the net horizontal currents on water transport. We used a fourth-order Runge-Kutta method for the temporal integration and a bilinear interpolation in space, which showed to be accurate enough in idealized and realistic applications (Delandmeter & Van Sebille, 2019; Lange & van Sebille, 2017). A time step of 158 s to balance accuracy and computational time was employed. It was also chosen to have the time step as an integer fraction of the M2 tidal period (44,714 s), which is the main tidal constituent in the DWS. In our setup, particles were released within the region of interest (denoted with the magenta contour in Figure 1) in the center of each of the 200 m \times 200 m grid cells but skipping every other cell, and their trajectories were integrated for 116 M2 periods (around 60 days). However, particles were not tracked anymore if they crossed the boundaries of the numerical domain before the integration time was reached. This procedure was repeated every M2 period from January-1980 to October-2015, with each release consisting of 12,967 particles. The total amount of particle trajectories obtained is (12,967 particles per deployment) \times (25,290 deployments) \approx 328 million particle trajectories (\approx 1.1 TB of data). To avoid deploying particles when most of the tidal flats are dry, the first deployment was near the time of maximum water volume within the DWS so that the subsequent ones (every M2 period) were also close to maximum volume conditions. Releasing only during high volume is not a strong limitation because particles deployed in shallow areas take several tidal periods to exit the system, so the LTTS of these particles are not very sensitive to the moment of release within the tidal cycle. The particle positions were saved every M2 period to remove the back-and-forth due to this dominant semidiurnal tidal constituent in the DWS (Zimmerman, 1976). We, thus, capture the net residual displacement of the particles. We note that individual tidal periods may deviate somewhat from the M2 period, but since M2 is the dominant constituent, the long-term mean tidal period equals the M2 period (Gerkema, 2019).

The particles behave as water parcels, so as the water level decreases from the moment of release, they travel with the flow and do not get stranded in the shallow areas located in the middle of the DWS or between every tidal inlet (see Figure 1). However, particles can get stuck when they are released too close to the coast or to areas that seldom flood, with the latter being more problematic because the initial water column in these regions at the moment of release can be close to the artificial minimum water depth employed by the GETM model. To avoid errors in the estimation of the LTTS due to these particles, we removed such particles from our original data set, ending up with around 283 million particle trajectories for our analysis (see Text S3 in Supporting Information S1 for details on the conditions used to remove the particles). To verify the robustness of our results, we evaluated the sensitivity of our Lagrangian simulation to the time step and the integration time employed (see Text S4 in Supporting Information S1).

2.2. Definitions of Lagrangian Transport Time Scales (LTTS)

The Lagrangian residence time is a function of space and time and highlights the spatio-temporal heterogeneity of transport. It is defined as the time required for a particle to exit a domain for the first time (Monsen et al., 2002; Zimmerman, 1976). Nonetheless, this first-crossing definition has a drawback. When particles are close to an open boundary, they might exit the system during ebb and return during flood, possibly repeating this behavior during the following cycles, after which they can remain in the domain for several days. In this way, such a definition of the residence time might give a wrong idea of the actual time particles spend in the system, particularly close to the inlets. We largely avoid this problem by saving particle positions only every M2 period (i.e., using the net or residual displacement). With those generated tracks, we define the Lagrangian residence time as the number of M2 periods required for the particles to leave our domain of interest (magenta contour in Figure 1) through its open boundaries. In other words, for the residence time, we count until the moment a particle crosses these open boundaries or until it reaches the maximum integration time (116 M2 \approx 60 d). Since the residence time varies in space and time, we define T_r^{ij} as the residence time of a particle released during the j -th deployment (at time t_j) at position (x_i, y_i) , where i is the spatial index of the particle released in the center of

the 200 m × 200 m grid, and t_j are the times of deployments (every M2 cycle during our 36-year simulation). However, once a particle leaves a system, it can come back at later stages. To capture this effect, we compute the Lagrangian exposure time T_e^{ij} , which is equal to the residence time plus the extra time the particle spends in the system after every return with a maximum value equal to the maximum integration time. Thus, $T_e^{ij} \geq T_r^{ij}$ (Huguet et al., 2019; Monsen et al., 2002).

To describe the spatial variability between seasons, we further define the temporal average over N_d^i deployments as

$$T_r^i = \frac{\sum_{j=1}^{N_d^i} T_r^{ij} H^{ij}}{\sum_{j=1}^{N_d^i} H^{ij}}, \quad (1)$$

where N_d^i is the total amount of deployments per point of release available during the time period for averaging, and H^{ij} is the height of the water column in which the particle is deployed. Specifically, we consider two temporal averages: one for all autumn-winter (September-February) and one for all spring-summer (March-August) seasons of our 36-year simulation. The weighted average using H^{ij} is employed because particles are advected with depth-averaged currents, and thus, a particle released over a large water column represents more fluid with that value of T_r^{ij} (Ridderinkhof & Zimmerman, 1990). To study the temporal variability of the system-wide LTTS, we define the average over all N_p^j particles released in our domain at the same time as

$$T_r^j = \frac{\sum_{i=1}^{N_p^j} T_r^{ij} H^{ij}}{\sum_{i=1}^{N_p^j} H^{ij}}, \quad (2)$$

where N_p^j is the total number of particles released inside our domain of interest at time t_j . Similarly, we obtain T_e^i and T_e^j using equivalents to Equation 1 and Equation 2 for the exposure time, respectively.

2.3. Atmospheric Forcing Characterization

To understand the origin of the variability of the LTTS, we characterize the atmospheric forcing using a local and a large-scale approach.

2.3.1. Local Approach

For the local approach, we employ the concept of sectorial wind energy, following Gerkema and Duran-Matute (2017). The wind direction is divided into eight sectors using the indices $s = 1, \dots, 8$, corresponding to southerly (S), southeasterly (SE), easterly (E), northeasterly (NE), northerly (N), northwesterly (NW), westerly (W), and southwesterly (SW) winds (i.e., the direction from which the wind blows). Then, the kinetic energy of an air parcel (wind energy) with mass m crossing a unit area A during an interval Δt and from sector or direction s is given by

$$E_{s,n} = \frac{1}{2} m W_{s,n}^2 = \frac{1}{2} \rho V W_{s,n}^2 = \frac{1}{2} \rho A \Delta t W_{s,n}^3, \quad (3)$$

where V is the volume, which is equal to the area A times the length $W_{s,n} \Delta t$; $W_{s,n}$ is the hourly wind speed (used in the GETM simulation) blowing from sector s , with n as a temporal index running over our full 36-year simulation; $\Delta t = 3,600$ s is the resolution of our wind data; and $\rho = 1.225$ kg m⁻³ is the density of the air at sea level with a temperature of 15°C.

In all our analysis, the wind energy from the grid point closest to the middle of the Texel inlet is employed. Due to the small spatial variations of the wind inside the DWS, we anticipate that using the wind energy from different locations does not change qualitatively our results, as was also the case for Duran-Matute et al. (2016) in their analysis of the residual volume transport in the DWS.

2.3.2. Large-Scale Approach

For the large-scale approach, we use the North Atlantic Oscillation (NAO), the East Atlantic Pattern (EAP), and the Scandinavian Pattern (SCAN). To derive them, we perform an empirical orthogonal function (EOF) analysis following Chafik et al. (2017) and Frederikse and Gerkema (2018). With this method, the atmospheric patterns have spatial structures represented by empirical orthogonal functions (EOFs), whereas their temporal variability are captured by principal components (PCs). To obtain the EOFs and PCs, we employ the monthly-mean sea level pressure (SLP) from the NCEP/NCAR Reanalysis 1 (Kalnay et al., 1996) during the period 1950–2015. For every grid cell, the monthly-mean SLP is detrended and deseasonalized, that is, the linear trend, and the annual and semi-annual components are removed. Then, the data are weighted by the cosine of the latitude at every grid point before computing the EOF analysis. This is done to give less weight to grid cells located toward the poles as they represent less area (which decreases with the cosine of the latitude in spherical coordinates). Finally, the EOF analysis is performed only in the North Atlantic/European sector (30°–80°N, 80W–50°E) to avoid the influence of external regions in the three main modes of variability obtained.

3. Results and Discussions

3.1. Seasonality and Interannual Variability of the LTTS

The mean autumn-winter and spring-summer spatial patterns for the residence time T_r^i (from Equation 1) are shown in Figures 2a and 2b, and in Figures 2c and 2d for the exposure time T_e^i . The lowest values are found near the inlets since they are the primary regions for exchange with the adjacent North Sea. Particles deployed around them leave the system in less than 1 week, with the corresponding areas being larger during autumn-winter. The highest values are found farther into the basins and mostly in the Western DWS (west of the Terschelling watershed). These values are up to a factor of two larger during spring-summer than during autumn-winter. Most of the particles deployed in the Western DWS during spring-summer tend to return to the DWS (see difference between T_e^i and T_r^i in the inset of Figure 2d). Nonetheless, during autumn-winter (inset of Figure 2c) this effect is observed only in the southernmost part of the domain. Thus, under a system-wide perspective, the variability of the LTTS is dominated by the Western DWS, which has a larger area and volume of water than the Eastern DWS and contains the longest and deepest channels. Consistent with all of the previously mentioned behavior, the wind roses show a marked difference between autumn-winter (Figure 2e) and spring-summer (Figure 2f), with the former exhibiting more frequent and stronger winds from the W, SW and S directions.

To get a representative seasonal cycle of the LTTS in the full DWS, we computed the spatial mean of the residence and exposures times (i.e., T_r^j and T_e^j from Equation 2). Then, the annual cycle for the residence and exposure times are estimated by fitting T_r^j and T_e^j to a model with a free constant and an annual harmonic. The system-wide annual signal of T_r^j varies from 10 to 11 days in November-January to 16–17 days in May-July, and for T_e^j from 14–16 days to 23–24 days, respectively (Figure 3). This means that the extra time that particles spend in the DWS system after they leave for the first time is smaller in November-January (around 4 days) than during May-July (around 7 days).

To understand the variability superimposed on the seasonal cycle, high-frequency effects (e.g., tides and energetic synoptic-scale events) from T_r^j (which has an M2 resolution) were removed by computing a 15-day mean, which is shown as \hat{T}_r in Figure 4a. Afterward, we performed a wavelet analysis (Torrence & Compo, 1998) of this spatially-averaged 15-day-mean residence time (\hat{T}_r), using the rectification of the bias proposed by Liu et al. (2007), to capture the localized time-frequency information in our time series. The wavelet power spectrum exhibits the strongest signal around the annual period (Figure 4b). However, anomalous behavior is still observed, with periods displaying a strong annual power (e.g., around 1983, 1990, 2000, and 2014) or a weak one (e.g., around 1986, 1996, 2006, and 2010). Similar results are obtained for the equivalent exposure time \hat{T}_e (Figure 5). Clearly, studies of the DWS based on time series of a few years, like those for 2009–2011 by Duran-Matute et al. (2014) and Duran-Matute et al. (2016), and for 2005–2015 by Donatelli et al. (2022a) and Donatelli et al. (2022b), cannot capture well this rich temporal variability of the system-wide transport characteristics.

The wavelet power spectrum of \hat{T}_r (Figure 4b) also contains significant power outside the annual signal, like the time spans with strong four-month periodicity around 1984, 1990, and 1997. There are also higher frequency events with a still significant signal but they are close to the background noise. These events cause large peaks with a relatively low persistence of only a few weeks. Thus, to focus on the system-wide low-frequency (seasonal

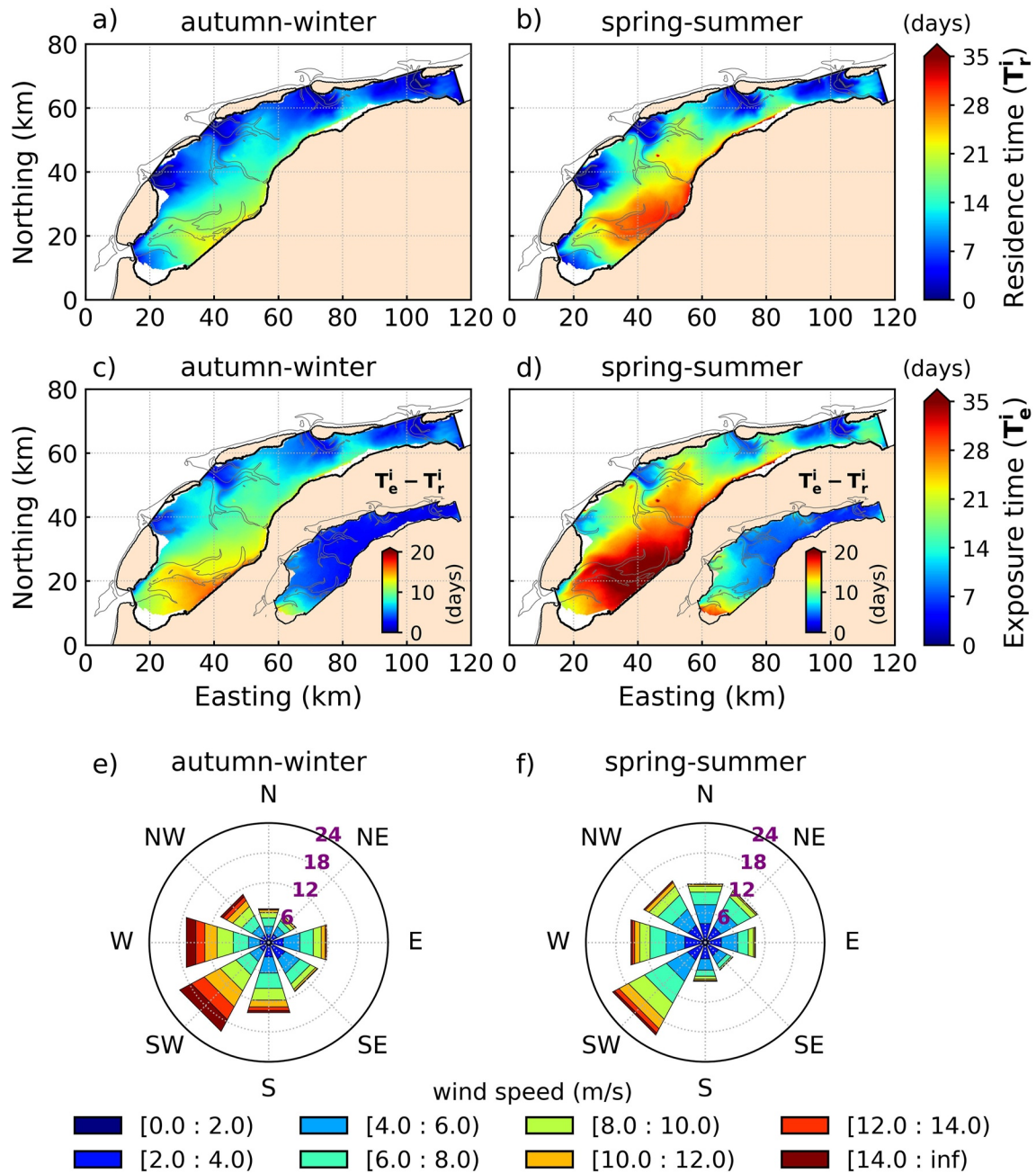


Figure 2. The time-averaged residence time T_r^i for (a) autumn-winter (September–February) and (b) spring-summer (March–August) based on the 36-year simulation; and the mean exposure time T_e^i for (c) autumn-winter (September–February) and (d) spring-summer (March–August). The insets in (c) and (d) show the difference between T_e^i and T_r^i . Regions in white within the DWS were removed from the analysis (see Section 2.1.2). The gray line indicates the -5 m isobath. (e) Autumn-winter and (f) spring-summer wind rose, in which the purple numbers indicate the percentage of time that the wind blows from a particular direction.

and interannual) variations of the LTTS and to find links with the wind forcing (which we discuss in Section 3.2) and large-scale circulation and atmospheric patterns (which will be addressed in Section 3.3), we filtered the time series. We removed variability from \hat{T}_r using a wavelet filter with a cutoff period of half a year. This procedure resulted in the half-year low-pass filtered signal of the spatially-averaged 15-day-mean residence time (\bar{T}_r) and exposure time (\bar{T}_e) (see Figures 4a and 5a, respectively). Most of the variability at low frequencies is due to the seasonal cycle. However, there are fluctuations at interannual time scales that modulate it. Clear examples are the anomalous winters (DJF) with the lowest \bar{T}_r (6–8 days) of 1983, 1990, 1995, 2000, 2007, 2008, and 2014 (using the year after December as the name of the winter); or the anomalous winters with the largest \bar{T}_r (12–16 days)

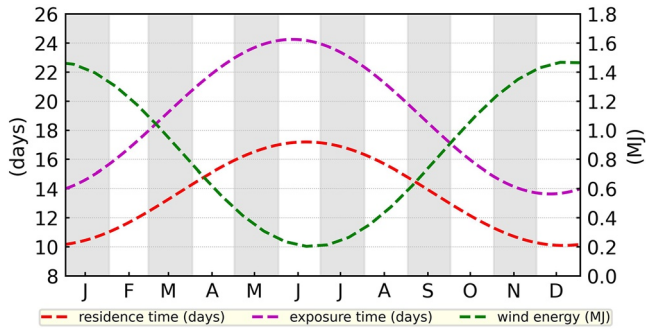


Figure 3. Annual cycle of the residence time (red), the exposure time (magenta), and the wind energy (green).

of 1996, 2003, 2006, 2009, and 2010. In summer (JJA), the variability of the peaks is less pronounced, with values that vary between 15 and 19 days. For \tilde{T}_e (Figure 5a), a similar behavior is observed during those winters, with the lowest values around 7–8 days and the largest between 16 and 26 days. During summer, \tilde{T}_e varies between 21 and 30 days.

3.2. Impact of the Wind on the System-Wide LTTS

To show the dominance of the wind on the variability of the LTTS, we propose a reconstruction of \tilde{T}_r (and an identical one for \tilde{T}_e) using the energy of the most dominant wind sectors (W, SW, and S). Winds from these directions are the most efficient for driving a strong residual flow from the Texel inlet to the Vlie inlet and the Terschelling watershed (Duran-Matute et al., 2014). We refer to this reconstruction as the *wind-based model* and is given by

$$\bar{T}_r = A e^{-\tilde{E}/B}, \quad (4)$$

where \tilde{E} is the sum of the half-year low-pass filter signal of the 15-day-mean wind energy of the dominant sectors (see Appendix A for the definition of the 15-day-mean wind energy per sector, and for the computation of \tilde{E}). Because \tilde{T}_r and \tilde{T}_e are quantities that depend on the future, the *wind-based model* employs \tilde{E} of the next 15-day interval in comparison to the LTTS time series. The constants A and B are fitting coefficients. The negative sign in the argument of the exponential reflects the anti-correlation between \tilde{T}_r and \tilde{E} (Figure 6a), which means that strong \tilde{E} conditions result in low \tilde{T}_r and \bar{T}_r ; while the opposite holds during weak \tilde{E} conditions. The constant $A = 18.38 \pm 0.15$ days (with 95% CI) for \bar{T}_r represents the maximum value that can be predicted with \bar{T}_r , which is reached during $\tilde{E} = 0$ conditions. This constant contains the mean effects of the residual tides, freshwater discharge, and other wind directions not included in the reconstruction. The constant $B = 2.61 \pm 0.07$ MJ is an e-folding wind energy scale for \bar{T}_r , which indicates that an increase in \tilde{E} equal to B would lead to a reduction

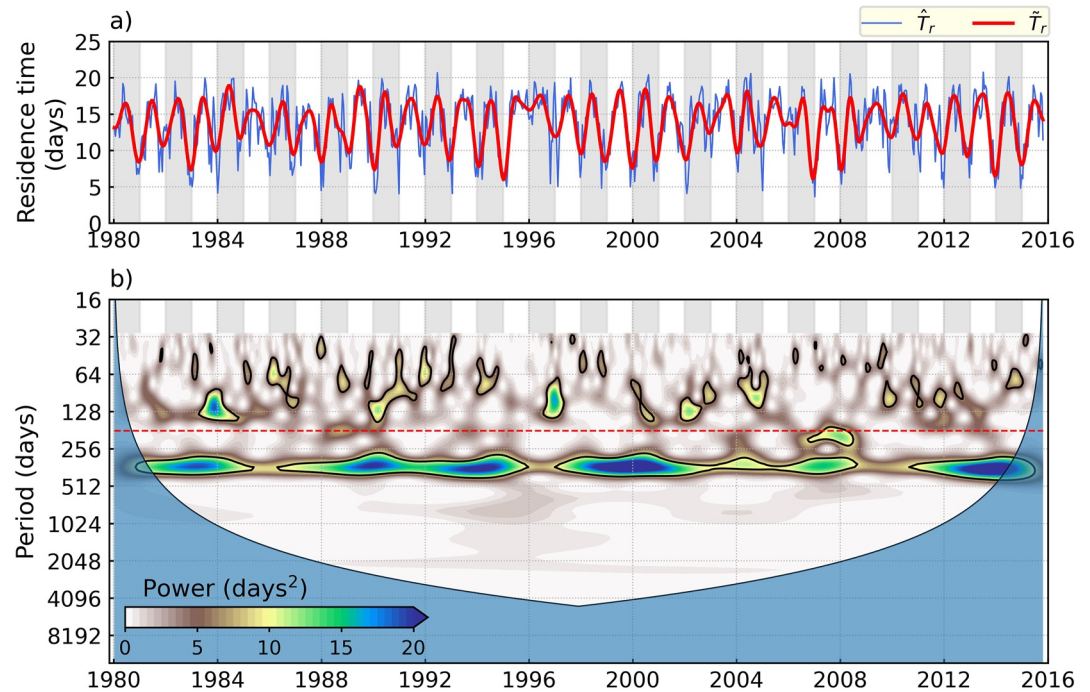


Figure 4. (a) Time series of the spatially-averaged 15-day-mean residence time (\hat{T}_r), and its half-year low-pass filtered component (\tilde{T}_r). (b) Wavelet power spectrum of \tilde{T}_r , where the black contour encloses regions with power greater than a lag-1 red-noise process with 95% confidence level; and the gray shadow region is the "cone of influence," where errors due to the finite length of the time series are present. The horizontal red dashed line highlights the half-year period employed as a cutoff for computing \tilde{T}_r .

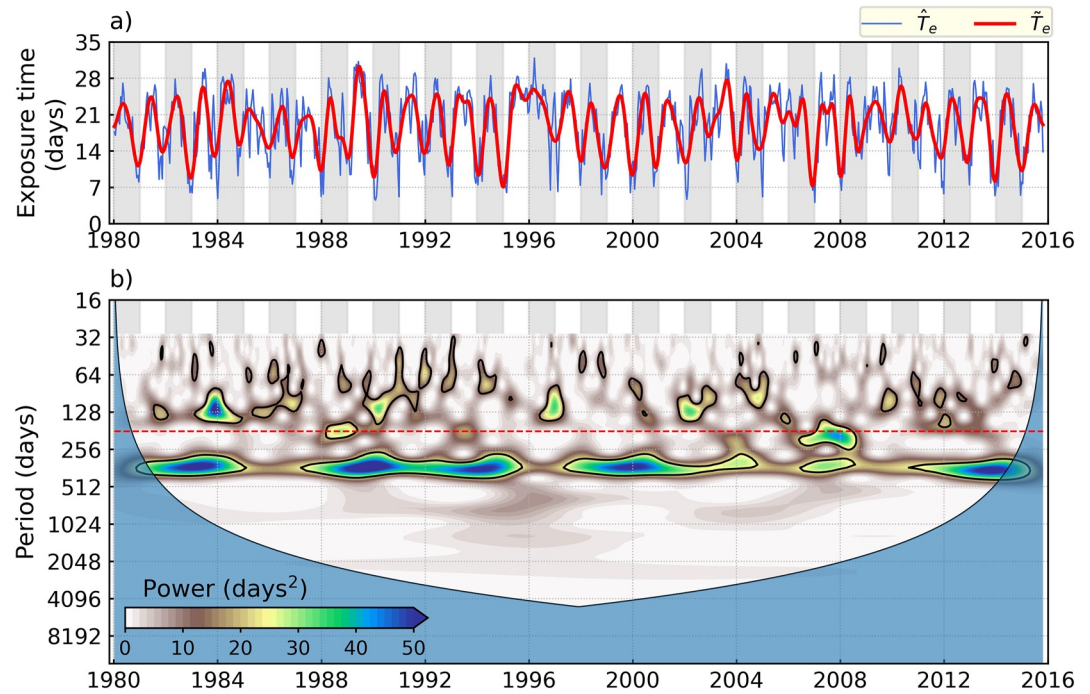


Figure 5. As in Figure 4, but for the exposure time.

of \bar{T}_r by 63%. For the exposure time, there is also a strong anti-correlation between \bar{T}_e and \bar{E} (Figure 6b). The maximum value predicted by \bar{T}_e is given by $A = 26.93 \pm 0.22$ days, and its e-folding wind energy scale is $B = 2.18 \pm 0.05$ MJ.

The values of \bar{T}_r (Figure 6a) match the numerical data quite well, with a Pearson correlation coefficient $R = 0.94$ and a root mean square error $RMSE = 1.02$ days (see Wilks (2011) for the definition of R and $RMSE$), with the latter representing 8% of the difference between the largest and lowest \bar{T}_r (13 days). Similar results are obtained for the exposure time (Figure 6b), with $R = 0.95$ and $RMSE = 1.45$ days, which represents 7% of the difference between the largest and lowest \bar{T}_e (23 days). These results reflect the capacity of the *wind-based model* to capture the seasonality, the energy transfer of most of the anomalous autumn-winter seasons to \bar{T}_r and \bar{T}_e , and some of the small spring-summer \bar{E} fluctuations that modify both time scales during these seasons.

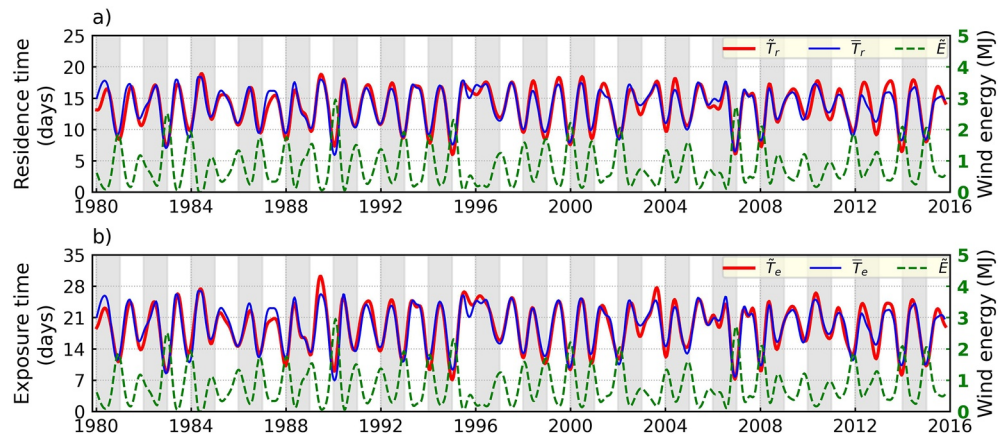


Figure 6. (a) Time series of the half-year low-pass filter of the spatially-averaged 15-day-mean residence time (\bar{T}_r), which is the same as the red line in Figure 5a; the reconstruction of \bar{T}_r using the *wind-based model* (\bar{T}_r , Equation 4); and the sum of the half-year low-pass filter of the 15-day-mean wind energy of the dominant wind sectors W + SW + S (\bar{E}). (b) Time series of the half-year low-pass filter of the spatially-averaged 15-day-mean exposure time (\bar{T}_e); the reconstruction of \bar{T}_e using the *wind-based model* (\bar{T}_e , instead of \bar{T}_r in Equation 4); and \bar{E} .

An exponential relationship between the residence time and the local forcing was also found in the Pearl River estuary (Sun et al., 2014), but with the freshwater discharge as predictor in this riverine-dominated estuary. The exponential model used in their study and in ours captures the asymptotic behavior of the TTS keeping physical values larger than zero during strong forcing conditions. For our case, the *wind-based model* can provide robust predictions if, for example, the model would be exposed to larger \tilde{E} values not seen during the fitting step. These attributes are hard to achieve with linear or polynomial models, which make the exponential one a good and simple tool to predict TTS.

An example of the ability of the *wind-based model* to capture anomalous \tilde{T}_r values is the winter of 1990. During this period, the lowest \tilde{T}_r is well reproduced, which is related to the largest \tilde{E} (3 MJ) of our 36-year record (Figure 6a). On the opposite side, we have the winter of 1996, which is a famous period in the North Sea region due to its low temperatures (Loewe, 1996). In this season, winds from the most dominant directions were unusually weak, but strong E winds were predominant, with most of their variability contained in periods of less than half a year. During this winter, \tilde{T}_r shows larger values than expected from the climatological winter months and exhibited closer values to the climatological summer months. The *wind-based model* (Figures 6a and 6b for \tilde{T}_r and \tilde{T}_e , respectively) suggests that the large values of the LTTS in winter of 1996 are explained by the weak wind energy from the usually dominant directions and not by the strong easterly winds observed (which are not explicitly included in the *wind-based model*).

The lack of strong influence of E winds on the LTTS in comparison to the predominant wind directions (SW quadrant) can be partly explained using the findings of Duran-Matute et al. (2014); Duran-Matute et al. (2016) and Donatelli et al. (2022a). They showed that strong winds from the SW quadrant (between 13 and 16 m/s) have an enormous potential to bring water inside the DWS from the North Sea. As a result, they can generate set-ups with tidally-averaged sea level in the DWS between 0.5 and 1.2 m, which triggers a residual circulation that favors the transport of water parcels across the tidal flats and shallow areas. These wind directions force the largest residual transport within the system, which is characterized by an inflow through the Texel inlet, and outflows from the Vlie inlet and the inlets located to the east of the Terschelling watershed (see Figure 1 to identify the locations of the inlets). Therefore, low values of the LTTS are induced.

On the other hand, strong E winds (around 13 m/s) can promote set-downs of up to 0.7 m, which reduces the tidally average volume inside the system by around 20%. These set-downs increase the exposure of most of the tidal flats and shallow areas during low tides and create a temporary system of independent tidal basins, which are connected during a small fraction of the tidal cycle (when the water level is high enough). Additionally, the geometry of the coast and the relative orientation of the inlets in the eastern part of the DWS with respect to the E winds, also contribute to avoid an efficient transport of water within the DWS and across its inlets. All these effects trigger an opposite circulation in comparison to the winds of the SW quadrant but with weaker intensity and weaker large-scale coherence, which is not strong enough to substantially affect the variability of the system-wide LTTS. This poor response of the LTTS to E winds is also related to the relative low persistence, frequency, and intensity of winds from this direction (as well as for the other non-dominant ones) in contrast to the winds from the SW quadrant (Figures 2e and 2f).

3.3. The Role of the Large-Scale Atmospheric Circulation and Patterns on the System-Wide LTTS

To investigate the role of the large-scale atmospheric circulation and patterns, we employ the monthly NCEP/NCAR Reanalysis 1 data set. It has a low spatial resolution (2.5° latitude \times 2.5° longitude), but an extended spatial coverage necessary to compute atmospheric patterns as in Chafik et al. (2017), whereas only the UERRA data set (due to its high spatial resolution of 11 km) was used to force the GETM simulation and obtain LTTS. The annual cycle of the large-scale wind in the subtropical North Atlantic is related to the seasonality (a meridional shift and change in intensity) of the Azores High and the semi-permanent Icelandic Low North Atlantic pressure systems (Trenberth et al., 1990) (Figure 7). This variability is transferred to the regional wind, which triggers a local wind response, and ultimately to the LTTS. As a result, a prevailing climatological wind energy (from the SW quadrant) is induced in the DWS, which was computed fitting the sum of the 15-day-mean wind energy of the dominant sectors (W + SW + S, see Equation A2 in Appendix A for the formal definition) to a model with a free constant and an annual harmonic. This signal is aligned with the geographical orientation of the system, and characterized by larger values in autumn-winter than in spring-summer (seven times more when contrasting the peaks in November-January with the lowest values in June-July, see Figure 3). Thus, it explains why the DWS is

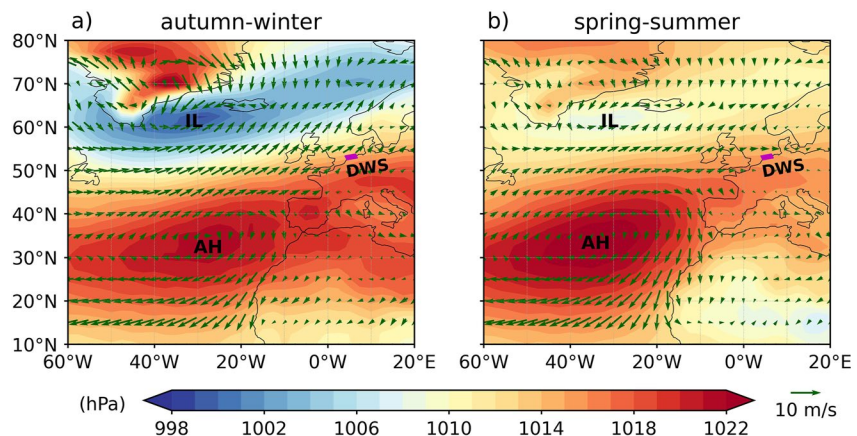


Figure 7. Mean sea level pressure and wind at 10 m above ground for (a) autumn-winter (September-February) and (b) spring-summer (March-August). These averages were obtained using the monthly NCEP/NCAR Reanalysis 1 data for the 1980–2015 period. To compute the winds, the mean wind direction is obtained from the angle of the average wind vector, whereas the mean wind speed is obtained from the average values of wind speed, which is the upper limit of the magnitude of the mean wind vector (Farrugia & Micallef, 2017). The small purple rectangle in panels (a)–(b) represents the DWS numerical domain. The location of the Azores High (AH) and Icelandic Low (IL) pressure systems are also highlighted.

at its most efficient climatological state for flushing in autumn-winter, which are the seasons when the LTTS are the lowest (Figures 2a, 2b, and 3).

Other low-frequency variations of the wind and sea level pressure, which are not explained by the seasonality, are mainly related to large-scale atmospheric patterns, such as the NAO, EAP, and SCAN (Frederikse & Gerkema, 2018). Therefore, our final objective is to determine if interannual variations of the LTTS in the DWS are driven by these large-scale patterns. First, we obtain the three leading modes of variability from the EOF analysis of the deseasonalized monthly-mean SLP in the North Atlantic region (see Section 2.3.2). Their spatial structure (EOFs) and their temporal variations (PCs) are shown in Figure 8, and they are very similar to those showed by Chafik et al. (2017) and Frederikse and Gerkema (2018). These first three modes at a monthly scale explain 32%, 17% and 15% of the SLP variability in the North Atlantic domain. They exhibit large-scale atmospheric structures that are akin to the NAO, EAP and SCAN teleconnection patterns. In comparison to the method used by the Climate Prediction Center (CPC, <https://www.cpc.ncep.noaa.gov/data/teledoc/telecontents.shtml>), our EOFs and the CPC teleconnection patterns are quite similar, but our PCs and the CPC indices are not necessarily fully interchangeable (Frederikse & Gerkema, 2018). A detailed description of our EOF results and their connection with the NAO, EAP, and SCAN are described in Text S5 in Supporting Information S1.

To link the interannual variations of \tilde{T}_r (and \tilde{T}_e) to the large-scale patterns, we remove the seasonal component from \tilde{T}_r , and then this deseasonalized or anomalous \tilde{T}_r was reconstructed using a multi-linear regression model. The predictors are based on the monthly PCs, which were interpolated to match the 15-day resolution of both LTTS, and then low-pass filtered using a cutoff period of half-year to remove high-frequency variations. We call this reconstruction the *PCs model*. Similar to the *wind-based model*, the PCs of the next 15-day interval are used as predictors. The reconstruction of \tilde{T}_r is obtained by joining the seasonal component with the *PCs model*. This combination is referred to as the *large-scale model* and is shown in Figure 9a; whereas the reconstruction of the deseasonalized \tilde{T}_r given by the *PCs model* is shown in Figure 9b. The *large-scale model* matched \tilde{T}_r quite well, with $R = 0.94$ and $\text{RMSE} = 0.99$ days. It also explains 96% of the variance of \tilde{T}_r (VAR_{exp} in Figure 9c), from which 72% is attributed to the seasonality, 21% to SCAN and NAO, and the remaining 3% to EAP. In general, the model captures most of the autumn-winter variability, but it has difficulties in reproducing the variations of the spring-summer peaks (Figure 9a), as was also the case for the *wind-based model* (Figure 6a). Similar results ($R = 0.92$ and $\text{RMSE} = 1.83$ days) and weak spring-summer predictability for the *large-scale model* are obtained for \tilde{T}_e (Figure 10).

The maximum predictability of the *PCs model* in terms of VAR_{exp} and R is found between November and February (Figure 9d), and it is mainly attributed to SCAN and NAO. This behavior is expected since the effects of the large-scale patterns are noticeable when the PCs show strong changes and largest values, which is more

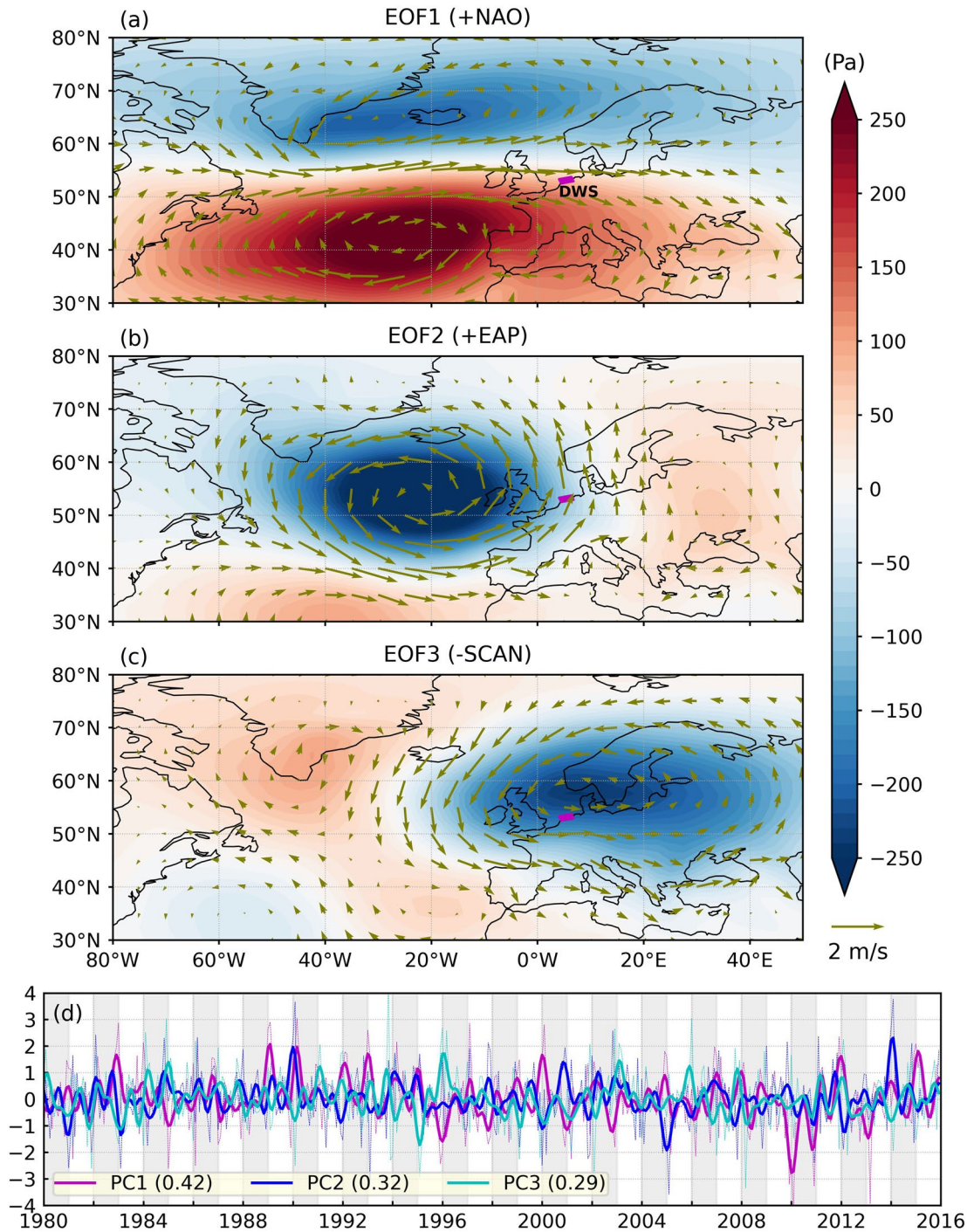


Figure 8. The three leading modes of the empirical orthogonal function (EOF) analysis based on the deseasonalized monthly-mean sea level pressure over the North Atlantic sector. (a)–(c) EOFs with units of Pressure (Pa), and (d) the monthly PCs (dotted lines) and their half-year low-pass filtered component (thick lines). The EOF and PC modes are defined following the common positive convention for NAO, EAP and SCAN (see the website of the Climate Prediction Center, <https://www.cpc.ncep.noaa.gov/data/teledoc/telecontents.shtml>). The first two EOFs (NAO and EAP) are displayed during their positive phases, whereas the third one (SCAN) is depicted during its negative phase. The geostrophic winds computed from the EOFs are depicted with arrows. The variance of the three monthly PCs (PC1 for NAO, PC2 for EAP, and PC3 for SCAN) is scaled to 1, and the numbers in the legend of (d) highlight the fraction of variance explained by the low-pass filtered PCs with respect to their monthly values. The small purple rectangle in panels (a)–(c) represents the DWS numerical domain.

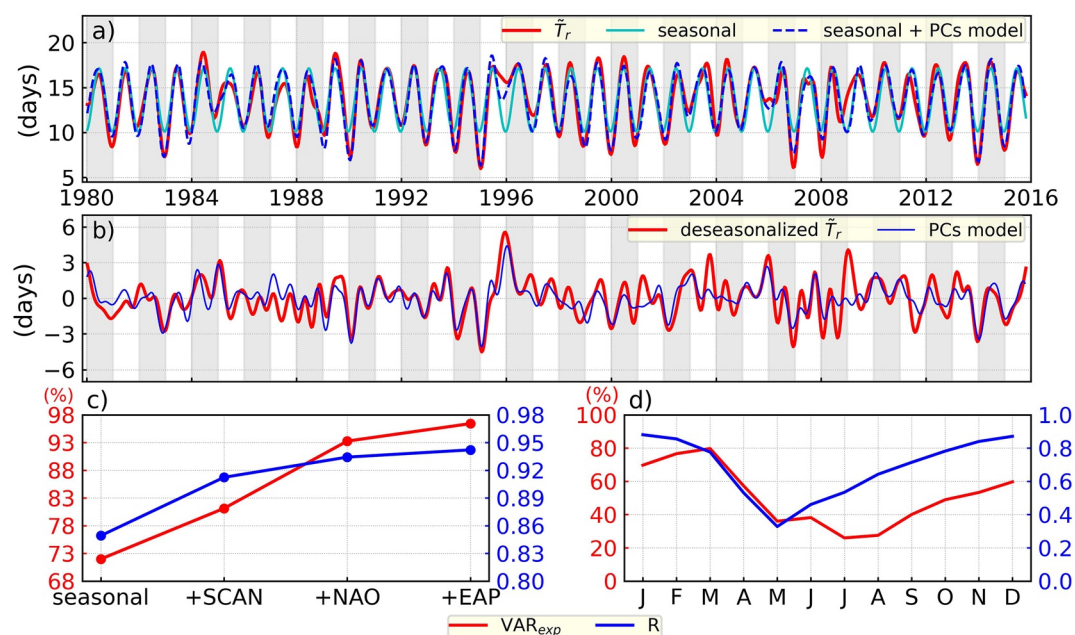


Figure 9. (a) Time series of the half-year low-pass filter of the spatially-averaged 15-day-mean residence time (\tilde{T}_r), its seasonal component, and its reconstruction with the *large-scale model* (seasonal + PCs model). (b) The deseasonalized \tilde{T}_r and its reconstruction with the PCs model. (c) Explained variance VAR_{exp} and correlation R for the reconstruction of \tilde{T}_r using cumulative components of the *large-scale model*: only the seasonal component; seasonal + SCAN (+SCAN); seasonal + SCAN + NAO (+NAO); and the *large-scale model*, that is, seasonal + SCAN + NAO + EAP (+EAP). The VAR_{exp} is defined as the ratio between the variance of the cumulative components of the *large-scale model* and the variance of \tilde{T}_r . (d) Monthly statistics (VAR_{exp} and R) of the reconstruction of the deseasonalized \tilde{T}_r with the PCs model. In this case, the VAR_{exp} is defined as the ratio between the variance of the PCs model and the variance of the deseasonalized \tilde{T}_r per month.

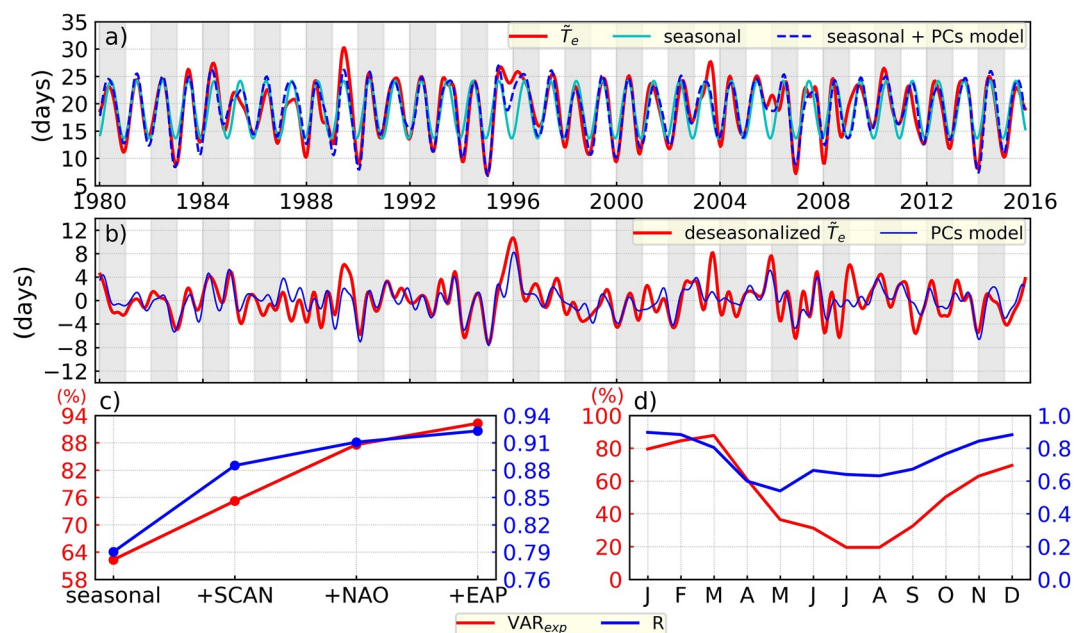


Figure 10. As in Figure 9, but for the exposure time.

common during autumn-winter (Figure 8d). The lowest \tilde{T}_r values observed during several autumn-winter seasons (Figure 9a) are predominantly associated with the interplay between negative SCAN, positive NAO, and positive EAP (Figure 8d), with the latter having the smallest contribution. The combination of their spatial patterns tends to induce along-coast anomalous winds (mostly from W and SW directions) that favor the flushing efficiency of the DWS system. This behavior is consistent with the study of Chafik et al. (2017), in which negative SCAN and positive NAO patterns explain most anomalous high monthly sea level values observed at several North Sea tidal gauge stations during autumn-winter. According to our results, they are concurrent with strong flushing conditions and with a low likelihood for the particles to return to the DWS (represented by low \tilde{T}_r and \tilde{T}_e , respectively).

Winters with the strongest flushing were well captured by the *PCs model* (Figures 9a and 9b). During the winters of 1990, 1995, 2007, and 2014, a decrease of \tilde{T}_r of around 3–4 days with respect to the December-January climatological value of 10 days was observed, which was related to high \tilde{E} (Figure 6a). Therefore, the lowest \tilde{T}_r values were induced by large-scale atmospheric patterns and not by storms, which induce high-frequency variations and are commonly associated with the presence of well-known weather regimes (Hochman et al., 2021). For example, during the well-known winter of 1990, two exceptionally strong storms (“Daria” and “Vivian”) passed over central Europe and crossed the North Sea in just few days (Pinto et al., 2009). As a result, they trigger the strongest hourly wind speeds from SW and W directions in our 36-year record (around 30 m/s or 60 MJ), but induced 15-day-mean peaks in the wind energy similar to other less stormy periods.

On the other hand, the most anomalous winters with the largest \tilde{T}_r values (1996 and 2006) were also well explained by the *PCs model*. During these winters, an increase of \tilde{T}_r of about 6 and 4 days with respect to the December-January climatology were observed, but the *PCs model* underestimated these values by around 1 day. The most extreme change between two consecutive winters (10 days for \tilde{T}_r and about 19 days for \tilde{T}_e) occurred between the winters of 1995–1996. In 1995, a combination of negative SCAN with positive NAO and EAP triggered a \tilde{E} stronger than its December-January climatology and induced one of the lowest \tilde{T}_r (around 6 days). The following year, the largest \tilde{T}_r during winter was observed (about 16 days). During this famous winter, positive SCAN and negative NAO induced strong E winds. However, as was stated in the previous section, the lack of \tilde{E} (and hence, the background forcing by the tides and freshwater discharge) is enough to explain why \tilde{T}_r during the winter of 1996 was similar to its May-July climatology. In agreement with this, during the winter of 2006 (and to a lesser extent for 2003, 2009, and 2010), \tilde{T}_r was also larger than its climatological value, which was related to quite low \tilde{E} , but also to low-frequency energy from the other directions.

During our period of analysis, the winter of 1996 is quite unique, as it was impacted by a strong negative NAO in a decade (1990–2000) with predominance of its positive phase (Hurrell & Deser, 2010). However, in the DWS only monitoring the NAO is not enough. In our record, the most negative NAO occurred during the winter of 2010 (Figure 8d) when the influence of SCAN was absent. However, it was during the winter of 1996 (with SCAN and NAO active) when the most anomalous \tilde{T}_r and \tilde{T}_e were observed (Figures 9 and 10b), which is consistent with the dominance of SCAN over NAO in the multi-decadal sea level variations along the southern North Sea (Frederikse & Gerkema, 2018).

3.4. Other Sources of Variability on the LTTS

Variations of the bathymetry were neglected in our simulation, which was done intentionally to isolate the role of the atmospheric forcing in our results. Relative stability in the location and orientation of the major channels connected to the Texel inlet has been observed since approximately 1972 or 40 years after the construction in 1932 of the Afsluitdijk (Elias et al., 2003, 2006), which is a closure dyke of around 30 km where the two main sluices feeding freshwater into the are located (Figure 1). Changes in the sedimentation-erosion patterns of the channels were observed in these studies, but with only minor modifications of the bathymetry profiles. Thus, during our period of analysis, we expect small effects of these bathymetry variations compared to the large effects of wind, particularly when focusing on the variability of system-wide LTTS, as is the case in most of our results.

The time series of the freshwater discharge from the sluice located at Den Oever is correlated with \tilde{E} ($R = 0.56$) and anti-correlated with \tilde{T}_r ($R = -0.68$) and \tilde{T}_e ($R = -0.61$); whereas for the sluice located at Kornwerderzand non-significant correlations are obtained. Because of this, it is not trivial to isolate the effect of both sluices on the variability of \tilde{T}_r and \tilde{T}_e under our current approach. However, it is known that the residual volume flow rate through the DWS during strong wind conditions from the dominant directions is one order of magnitude

larger than the one associated with the tides and the freshwater discharge (Duran-Matute et al., 2014), and that the total freshwater discharge of both sluices can only explain less than 5% of the variability of the residual transport in this system (Donatelli et al., 2022a). Therefore, we expect that the freshwater discharge and the residual tidal currents are the main factors controlling the background \tilde{T}_r ($A = 18.38$ days) and \tilde{T}_e ($A = 26.93$ days), which are obtained when the wind energy of the most energetic sectors (\tilde{E}) is null in the *wind-based model*. In addition, these forcing mechanisms also seem to explain part of the variability of \tilde{T}_r and \tilde{T}_e not explained by the *wind-based model* and the *large-scale model* during calm conditions (mainly spring-summer months), which are the periods in which both of these models show strong lack of predictability.

Because our main results are based on the characterization of the system-wide LTTS, the vertical structure of the LTTS was ignored using depth-averaged currents. Locally, there might be a marked heterogeneity in this vertical structure (Du & Shen, 2016; Wolk, 2003), which might be associated to, for example, a strong gravitational circulation and wind-driven shear effects. However, it is not currently feasible to perform a 3D Lagrangian analysis for 36-year of the DWS due to the amount of data required to compute the necessary 3D particle trajectories. Nonetheless, our results can be useful to select, simulate, and understand the 3D behavior of the LTTS during particular and striking conditions, like the transition between the winters with strong and weak winds from the most energetic directions in 1995–1996. Moreover, care should be taken with the values of the LTTS during cold winters as a module of ice was not considered in our GETM setup. We expect that the presence of ice further reduces the values of the LTTS. The presence of ice was reported in several basins of the Wadden Sea system during the cold winter of 1996 (Martens, 2001), and during other winters like in 1986 (Van Duyl & Kop, 1990), and 2012 and 2013 (Donker et al., 2015).

4. Conclusions

While it has been acknowledged that high-frequency events, like storms crossing the Dutch Wadden Sea (DWS) in few days or bora winds in the Venice lagoon, can completely renew the water in multiple-inlet systems, we show here that low-frequency wind variability can also play a large role in modulating the transport time scales in a multiple-inlet system. The broad and immediate implication of our results is that interannual changes in the atmospheric patterns can have a much larger effect on the variations of the water transport than may have been expected, and hence, on the long-term ecology and functioning of multiple-inlet systems.

For the case of the DWS, the lowest system-wide Lagrangian transport time scales (LTTS) are observed in several years during autumn-winter months and are well explained by the concurrent negative phase of the Scandinavia Pattern (SCAN) and the positive phase of the North Atlantic Oscillation (NAO), which induce stronger SW and W winds in this system. These winds trigger an anomalous eastward flow that enhances the flushing efficiency, which is typically already strong in autumn-winter. The opposite happens during positive SCAN and negative NAO, and weaker flushing during autumn-winter is observed. In contrast to single-inlet systems (like in the study of Du and Shen (2016)), our results show that system-wide LTTS in multiple-inlet systems, like the DWS, are representative of the overall system when studying the influence of winds on the seasonal and interannual variations of the LTTS. This response is in agreement with the fact that winds from specific intensities and directions are very efficient in forcing net residual transport across watersheds (i.e., tidal divides) and through the inlets of multiple-inlet systems (Duran-Matute et al., 2016; Li, 2013). A similar response can be expected in other wind-dominated multiple-inlet systems (e.g., along the North Sea coast), leading to seasonal and interannual variations of the LTTS driven by the large-scale circulation and atmospheric patterns, respectively.

Our findings also reveal that care should be taken when observing variations of the long-term values of the residual volume flow rate across inlets and watersheds, when events with strong wind conditions (like storms) affect a coastal area. Using a simulation of the DWS for the years 2005–2015, Donatelli et al. (2022a) attributed changes in the long-term residual volume transport to moderate winds and storms. According to our results, this does not necessarily indicate that extreme events are responsible for these long-term variations. Instead, we expect that the long-term variability of the residual flow rate in other wind-dominated multiple-inlet systems is also (at least partly) driven by large-scale atmospheric patterns, as was the case for the interannual variations of the LTTS in the DWS (from our current study), and for the multi-decadal sea level variability along the North Sea coastal areas (Frederikse & Gerkema, 2018).

Finally, our study highlights the importance of understanding the water transport variability due to local and remote forcing to, for example, explain better why large-scale atmospheric patterns affect biological processes

(see e.g., Golubkov & Golubkov, 2021; Straile & Adrian, 2000), and to improve analytical models that use TTS to model ecological processes (see e.g., Lucas & Deleersnijder, 2020). From a practical point of view, analytical models like those proposed here to predict the system-wide LTTS using the wind and the large-scale atmospheric patterns as predictors, could be employed to estimate LTTS during periods not covered by such detailed simulations, particularly, for seasonal forecasts and future climate-change scenarios.

Appendix A: Wind Energy Averaging

To establish connections with the LTTS and to smooth the noisy, hourly, high-resolution wind energy data from Equation 3, and to remove most of the high-frequency effects (e.g., storms), we compute the mean wind energy during 15-day intervals. For a given sectorial direction s , the 15-day-mean wind energy is defined as

$$\hat{E}_s = N^{-1} \sum_n E_{s,n} = \frac{1}{2} \rho A \Delta t N^{-1} \sum_n W_{s,n}^3 = C \Delta t N^{-1} \sum_n W_{s,n}^3, \quad (\text{A1})$$

where $N = 360$ is the total amount of hourly data points in a 15-day interval, $\Delta t = 3,600$ s, $C = \frac{1}{2} \rho A = 0.6125$ kg m⁻¹, and the total wind energy is obtained from $\hat{E}_T = \sum_s \hat{E}_s = C \Delta t N^{-1} \sum_n W_n^3$, where $W_n^3 = \sum_s W_{s,n}^3$ is the cube of the hourly wind speed. A similar expression to Equation A1, but for yearly averages, was used by Gerkema and Duran-Matute (2017), and Donatelli et al. (2022a).

The sum of the wind energy of the most energetic sectors (W + SW + S) is obtained from Equation A1 yielding

$$\hat{E} = \hat{E}_W + \hat{E}_{SW} + \hat{E}_S. \quad (\text{A2})$$

This time series, with a 15-day resolution, was employed to compute the annual cycle of the wind energy showed in Figure 3.

Then, we apply a half-year low-pass filter to each \hat{E}_s (Equation A1), as was done for the LTTS, which we call \tilde{E}_s . Due to the undulatory nature of the wavelet filter (and other similar ones like the Lanczos filter) and to the fact that \hat{E}_s could be near zero, slightly negative values appear after filtering. To be physically correct, we set all negative values of \tilde{E}_s to zero. Finally, we add \tilde{E}_s from the most energetic sectors (W + SW + S), and get \tilde{E} , which we call the sum of the half-year low-pass filter of the 15-day-mean wind energy of the dominant sectors. Almost identical results are obtained if we apply the low-pass filter directly to \hat{E} defined in Equation A2.

To put values into context, at an hourly time scale (the resolution of the wind), maximum peaks of around 60 MJ are observed from the SW quadrant, which corresponds to winds of around 30 m/s. At a 15-day-mean time scale, maximum peaks of around 6 MJ are obtained for \hat{E} . This is equivalent to a wind (assuming identical persistent wind conditions) of about 14 m/s, which is computed using $(\hat{E}/(C \Delta t))^{1/3}$. For \tilde{E} , peaks of 3 MJ are obtained (Figure 6), which correspond to a wind of around 11 m/s. Finally, the 1.45 MJ peak for the annual cycle of the wind energy (Figure 3), would be equivalent to a wind of around 9 m/s, which is close to the value observed when computing the seasonal cycle of the wind for the SW quadrant.

Conflict of Interest

The authors declare no conflicts of interest relevant to this study.

Data Availability Statement

Data and scripts (based on Python v3.8) used to reproduce the figures of this study are available in the GitHub repository https://github.com/JeancarloFU/paper_Atmospherically_Driven_Seasonal_Interannual_LTTS_Multi-pleInlet. The data are also archived in 4TU.ResearchData at <https://doi.org/10.4121/21187324> (Fajardo-Urbina et al., 2023). The wavelet analysis is based on the Python package Pycwt v0.3.0a22 (<https://anaconda.org/conda-forge/pycwt>), but we added a script to perform the bias correction (Liu et al., 2007) and a wavelet filter (Torrence & Compo, 1998). Monthly-mean sea level pressure and wind at 10 m above ground were obtained from The NCEP-NCAR Reanalysis 1 data, which is provided by the NOAA PSL, Boulder, Colorado, USA, from their website at <https://psl.noaa.gov/data/gridded/data.ncep.reanalysis.html>. Eulerian data was produced with the

GETM/GOTM model, and its set-up is described in Duran-Matute et al. (2014) and Gräwe et al. (2016). The Lagrangian model (Parcels v2.1.1) can be downloaded from <https://anaconda.org/conda-forge/parcels> or <https://oceanparcels.org>.

Acknowledgments

This study was financially supported by the NWO/ENW project: "The Dutch Wadden Sea as an event-driven system: long-term consequences for exchange (LOCO-EX)" (OCENW.KLEIN.138). The numerical simulations with GETM were done thanks to the North-German Supercomputing Alliance (HLRN).

References

- Burchard, H., & Bolding, K. (2002). GETM - A general estuarine transport model. Scientific documentation, Tech. Rep. EUR, 20253 EN.
- Chafik, L., Nilsen, J. E. Ø., & Dangendorf, S. (2017). Impact of North Atlantic teleconnection patterns on Northern European sea level. *Journal of Marine Science and Engineering*, 5(3), 43. <https://doi.org/10.3390/jmse5030043>
- Cimatoribus, A., Lemmin, U., & Barry, D. (2019). Tracking Lagrangian transport in Lake Geneva: A 3D numerical modeling investigation. *Limnology & Oceanography*, 64(3), 1252–1269. <https://doi.org/10.1002/lno.11111>
- Cucco, A., & Umgiesser, G. (2006). Modeling the Venice Lagoon residence time. *Ecological Modelling*, 193(1–2), 34–51. <https://doi.org/10.1016/j.ecolmodel.2005.07.043>
- Cucco, A., Umgiesser, G., Ferrarin, C., Perilli, A., Canu, D. M., & Solidoro, C. (2009). Eulerian and Lagrangian transport time scales of a tidal active coastal basin. *Ecological Modelling*, 220(7), 913–922. <https://doi.org/10.1016/j.ecolmodel.2009.01.008>
- Defne, Z., & Ganju, N. K. (2015). Quantifying the residence time and flushing characteristics of a shallow, back-barrier estuary: Application of hydrodynamic and particle tracking models. *Estuaries and Coasts*, 38(5), 1719–1734. <https://doi.org/10.1007/s12237-014-9885-3>
- Delandmeter, P., & Van Sebille, E. (2019). The parcels v2. 0 Lagrangian framework: New field interpolation schemes. *Geoscientific Model Development*, 12(8), 3571–3584. <https://doi.org/10.5194/gmd-12-3571-2019>
- den Heyer, C., & Kalf, J. (1998). Organic matter mineralization rates in sediments: A within-and among-lake study. *Limnology & Oceanography*, 43(4), 695–705. <https://doi.org/10.4319/lno.1998.43.4.0695>
- Dippner, J. W., Bartl, I., Chrysagi, E., Holtermann, P., Kremp, A., Thoms, F., & Voss, M. (2019). Lagrangian residence time in the Bay of Gdańsk, Baltic Sea. *Frontiers in Marine Science*, 725. <https://doi.org/10.3389/fmars.2019.00725>
- Donatelli, C., Duran-Matute, M., Gräwe, U., & Gerkema, T. (2022a). Residual circulation and freshwater retention within an event-driven system of intertidal basins. *Journal of Sea Research*, 186, 102242. <https://doi.org/10.1016/j.seares.2022.102242>
- Donatelli, C., Duran-Matute, M., Gräwe, U., & Gerkema, T. (2022b). Statistical detection of spatio-temporal patterns in the salinity field within an inter-tidal basin. *Estuaries and Coasts*, 45(8), 1–18. <https://doi.org/10.1007/s12237-022-01089-3>
- Donker, J., Van der Vegt, M., & Hoekstra, P. (2015). Erosion of an intertidal mussel bed by ice-and wave-action. *Continental Shelf Research*, 106, 60–69. <https://doi.org/10.1016/j.csr.2015.07.007>
- Du, J., & Shen, J. (2016). Water residence time in Chesapeake Bay for 1980–2012. *Journal of Marine Systems*, 164, 101–111. <https://doi.org/10.1016/j.jmarsys.2016.08.011>
- Duran-Matute, M., Gerkema, T., De Boer, G., Nauw, J., & Gräwe, U. (2014). Residual circulation and freshwater transport in the Dutch Wadden Sea: A numerical modelling study. *Ocean Science*, 10(4), 611–632. <https://doi.org/10.5194/os-10-611-2014>
- Duran-Matute, M., Gerkema, T., & Sassi, M. G. (2016). Quantifying the residual volume transport through a multiple-inlet system in response to wind forcing: The case of the western Dutch Wadden Sea. *Journal of Geophysical Research: Oceans*, 121(12), 8888–8903. <https://doi.org/10.1002/2016JC011807>
- Elias, E., Cleveringa, J., Buijsman, M., Roelvink, J., & Stive, M. (2006). Field and model data analysis of sand transport patterns in Texel tidal inlet (The Netherlands). *Coastal Engineering*, 53(5–6), 505–529. <https://doi.org/10.1016/j.coastaleng.2005.11.006>
- Elias, E., Stive, M., Bonekamp, H., & Cleveringa, J. (2003). Tidal inlet dynamics in response to human intervention. *Coastal Engineering Journal*, 45(04), 629–658. <https://doi.org/10.1142/S0578563403000932>
- Fajardo-Urbina, J. M., Duran-Matute, M., Clercq, H. J., Gerkema, T., Gräwe, U., & Arts, G. (2023). Data for reproducing the figures from the manuscript "Atmospherically driven seasonal and interannual variability in the Lagrangian transport time scales of a multiple-inlet coastal system" [Dataset]. 4TU.ResearchData. <https://doi.org/10.4121/21187324>
- Farrugia, P. S., & Micallef, A. (2017). Vectorial statistics for the standard deviation of wind direction. *Meteorology and Atmospheric Physics*, 129(5), 495–506. <https://doi.org/10.1007/s00703-016-0483-8>
- Frederikse, T., & Gerkema, T. (2018). Multi-decadal variability in seasonal mean sea level along the North Sea coast. *Ocean Science*, 14(6), 1491–1501. <https://doi.org/10.5194/os-14-1491-2018>
- Gerkema, T. (2019). *An introduction to tides*. Cambridge University Press.
- Gerkema, T., & Duran-Matute, M. (2017). Interannual variability of mean sea level and its sensitivity to wind climate in an inter-tidal basin. *Earth System Dynamics*, 8(4), 1223–1235. <https://doi.org/10.5194/esd-8-1223-2017>
- Golubkov, M., & Golubkov, S. (2021). Relationships between northern hemisphere teleconnection patterns and phytoplankton productivity in the Neva Estuary (northeastern Baltic Sea). *Frontiers in Marine Science*, 8, 735790. <https://doi.org/10.3389/fmars.2021.735790>
- González, F. U. T., Herrera-Silveira, J. A., & Aguirre-Macedo, M. L. (2008). Water quality variability and eutrophic trends in karstic tropical coastal lagoons of the Yucatán Peninsula. *Estuarine, Coastal and Shelf Science*, 76(2), 418–430. <https://doi.org/10.1016/j.ecss.2007.07.025>
- Gräwe, U., Flüser, G., Gerkema, T., Duran-Matute, M., Badewien, T. H., Schulz, E., & Burchard, H. (2016). A numerical model for the entire Wadden Sea: Skill assessment and analysis of hydrodynamics. *Journal of Geophysical Research: Oceans*, 121(7), 5231–5251. <https://doi.org/10.1002/2016JC011655>
- Hailegeorgis, D., Lachkar, Z., Rieper, C., & Gruber, N. (2021). A Lagrangian study of the contribution of the Canary coastal upwelling to the nitrogen budget of the open North Atlantic. *Biogeosciences*, 18(1), 303–325. <https://doi.org/10.5194/bg-18-303-2021>
- Herrling, G., & Winter, C. (2015). Tidally-and wind-driven residual circulation at the multiple-inlet system east Frisian Wadden sea. *Continental Shelf Research*, 106, 45–59. <https://doi.org/10.1016/j.csr.2015.06.001>
- Hochman, A., Messori, G., Quinting, J. F., Pinto, J. G., & Grams, C. M. (2021). Do Atlantic-European weather regimes physically exist? *Geophysical Research Letters*, 48(20), e2021GL095574. <https://doi.org/10.1029/2021GL095574>
- Huguet, J.-R., Brenon, I., & Coulombier, T. (2019). Characterisation of the water renewal in a macro-tidal marina using several transport time-scales. *Water*, 11(10), 2050. <https://doi.org/10.3390/w11102050>
- Hurrell, J. W., & Deser, C. (2010). North Atlantic climate variability: The role of the North Atlantic oscillation. *Journal of Marine Systems*, 79(3–4), 231–244. <https://doi.org/10.1016/j.jmarsys.2009.11.002>
- Jiang, L., Soetaert, K., & Gerkema, T. (2019). Decomposing the intra-annual variability of flushing characteristics in a tidal bay along the North Sea. *Journal of Sea Research*, 155, 101821. <https://doi.org/10.1016/j.seares.2019.101821>

- Kalnay, E., Kanamitsu, M., Kistler, R., Collins, W., Deaven, D., Gandin, L., et al. (1996). The NCEP/NCAR 40-year reanalysis project. *Bulletin of the American Meteorological Society*, 77(3), 437–472. [https://doi.org/10.1175/1520-0477\(1996\)077<0437:TNYRP>2.0.CO;2](https://doi.org/10.1175/1520-0477(1996)077<0437:TNYRP>2.0.CO;2)
- Lange, M., & van Sebille, E. (2017). Parcels v0.9: Prototyping a Lagrangian ocean analysis framework for the petascale age. *Geoscientific Model Development*, 10(11), 4175–4186. <https://doi.org/10.5194/gmd-10-4175-2017>
- Li, C. (2013). Subtidal water flux through a multiple-inlet system: Observations before and during a cold front event and numerical experiments. *Journal of Geophysical Research: Oceans*, 118(4), 1877–1892. <https://doi.org/10.1002/jgrc.20149>
- Liu, Y., San Liang, X., & Weisberg, R. H. (2007). Rectification of the bias in the wavelet power spectrum. *Journal of Atmospheric and Oceanic Technology*, 24(12), 2093–2102. <https://doi.org/10.1175/2007JTECHO511.1>
- Loewe, P. (1996). Surface temperatures of the North Sea in 1996. *Deutsche Hydrografische Zeitschrift*, 48(2), 175–184. <https://doi.org/10.1007/BF02799386>
- Lucas, L. V., & Deleersnijder, E. (2020). Timescale methods for simplifying, understanding and modeling biophysical and water quality processes in coastal aquatic ecosystems: A review. *Water*, 12(10), 2717. <https://doi.org/10.3390/w12102717>
- Martens, P. (2001). Effects of the severe winter 1995/96 on the biological oceanography of the Sylt-Rømø tidal basin. *Helgolander Marine Research*, 55(3), 166–169. <https://doi.org/10.1007/s101520100078>
- Monsen, N. E., Cloern, J. E., Lucas, L. V., & Monismith, S. G. (2002). A comment on the use of flushing time, residence time, and age as transport time scales. *Limnology & Oceanography*, 47(5), 1545–1553. <https://doi.org/10.4319/lo.2002.47.5.1545>
- Patgaonkar, R. S., Vethamony, P., Lokesh, K., & Babu, M. (2012). Residence time of pollutants discharged in the Gulf of Kachchh, northwestern Arabian Sea. *Marine Pollution Bulletin*, 64(8), 1659–1666. <https://doi.org/10.1016/j.marpolbul.2012.05.033>
- Pawlowicz, R., Hannah, C., & Rosenberger, A. (2019). Lagrangian observations of estuarine residence times, dispersion, and trapping in the Salish Sea. *Estuarine, Coastal and Shelf Science*, 225, 106246. <https://doi.org/10.1016/j.ecss.2019.106246>
- Pinto, J. G., Zacharias, S., Fink, A. H., Leckebusch, G. C., & Ulbrich, U. (2009). Factors contributing to the development of extreme North Atlantic cyclones and their relationship with the NAO. *Climate Dynamics*, 32(5), 711–737. <https://doi.org/10.1007/s00382-008-0396-4>
- Rayson, M. D., Gross, E. S., Hetland, R. D., & Fringer, O. B. (2016). Time scales in Galveston Bay: An unsteady estuary. *Journal of Geophysical Research: Oceans*, 121(4), 2268–2285. <https://doi.org/10.1002/2015JC011181>
- Ridal, M., Olsson, E., Uden, P., Zimmermann, K., & Ohlsson, A. (2017). Uncertainties in ensembles of regional re-analyses. Deliverable D2.7 HARMONIE reanalysis report of results and dataset. Retrieved from <http://www.uerra.eu/component/dpattachments/?task=attachment.download&id=296>
- Ridderinkhof, H., & Zimmerman, J. (1990). Mixing processes in a numerical model of the Western Dutch Wadden Sea. In *Residual currents and long-term transport* (pp. 194–209). Springer. https://doi.org/10.1007/978-1-4613-9061-9_15
- Safak, I., Wiberg, P., Richardson, D., & Kurum, M. (2015). Controls on residence time and exchange in a system of shallow coastal bays. *Continental Shelf Research*, 97, 7–20. <https://doi.org/10.1016/j.csr.2015.01.009>
- Sassi, M. G., Gerkema, T., Duran-Matute, M., & Nauw, J. J. (2016). Residual water transport in the marsdiep tidal inlet inferred from observations and a numerical model. *Journal of Marine Research*, 74(1), 21–42. Retrieved from https://elischolar.library.yale.edu/journal_of_marine_research/413
- Schwichtenberg, F., Callies, U., & van Beusekom, J. E. (2017). Residence times in shallow waters help explain regional differences in Wadden Sea eutrophication. *Geo-Marine Letters*, 37(2), 171–177. <https://doi.org/10.1007/s00367-016-0482-2>
- Soomere, T., Andrejev, O., Myrberg, K., & Sokolov, A. (2011). The use of Lagrangian trajectories for the identification of the environmentally safe fairways. *Marine Pollution Bulletin*, 62(7), 1410–1420. <https://doi.org/10.1016/j.marpolbul.2011.04.041>
- Straile, D., & Adrian, R. (2000). The North Atlantic Oscillation and plankton dynamics in two European lakes: Two variations on a general theme. *Global Change Biology*, 6(6), 663–670. <https://doi.org/10.1046/j.1365-2486.2000.00350.x>
- Sun, J., Lin, B., Li, K., & Jiang, G. (2014). A modelling study of residence time and exposure time in the Pearl River estuary, China. *Journal of Hydro-Environment Research*, 8(3), 281–291. <https://doi.org/10.1016/j.jher.2013.06.003>
- Torrence, C., & Compo, G. P. (1998). A practical guide to wavelet analysis. *Bulletin of the American Meteorological Society*, 79(1), 61–78. [https://doi.org/10.1175/1520-0477\(1998\)079<0061:APGTWA>2.0.CO;2](https://doi.org/10.1175/1520-0477(1998)079<0061:APGTWA>2.0.CO;2)
- Trenberth, K. E., Large, W. G., & Olson, J. G. (1990). The mean annual cycle in global ocean wind stress. *Journal of Physical Oceanography*, 20(11), 1742–1760. [https://doi.org/10.1175/1520-0485\(1990\)020<1742:TMACIG>2.0.CO;2](https://doi.org/10.1175/1520-0485(1990)020<1742:TMACIG>2.0.CO;2)
- Van Duyl, F., & Kop, A. (1990). Seasonal patterns of bacterial production and biomass in intertidal sediments of the western Dutch Wadden Sea. *Marine Ecology Progress Series*, 59, 249–261. <https://doi.org/10.3354/meps059249>
- Wilks, D. S. (2011). *Statistical methods in the atmospheric sciences* (Vol. 100). Academic press
- Wolk, F. (2003). *Three-dimensional Lagrangian tracer modelling in Wadden sea areas* (Diploma thesis). Carl von Ossietzky University Oldenburg.
- Xiong, J., Shen, J., Qin, Q., & Du, J. (2021). Water exchange and its relationships with external forcings and residence time in Chesapeake Bay. *Journal of Marine Systems*, 215, 103497. <https://doi.org/10.1016/j.jmarsys.2020.103497>
- Zhang, W. G., Wilkin, J. L., & Schofield, O. M. (2010). Simulation of water age and residence time in New York Bight. *Journal of Physical Oceanography*, 40(5), 965–982. <https://doi.org/10.1175/2009JPO4249.1>
- Zimmerman, J. T. F. (1976). Mixing and flushing of tidal embayments in the western Dutch Wadden Sea part I: Distribution of salinity and calculation of mixing time scales. *Netherlands Journal of Sea Research*, 10(2), 149–191. [https://doi.org/10.1016/0077-7579\(76\)90013-2](https://doi.org/10.1016/0077-7579(76)90013-2)